



Effects of ambient CO₂ and H₂O on soot processes in n-dodecane spray combustion using large eddy simulation

Zhang, Min; Ong, Jiun Cai; Pang, Kar Mun; Bai, Xue-Song; Walther, Jens H.

Published in:
Fuel

Link to article, DOI:
[10.1016/j.fuel.2021.122700](https://doi.org/10.1016/j.fuel.2021.122700)

Publication date:
2022

Document Version
Publisher's PDF, also known as Version of record

[Link back to DTU Orbit](#)

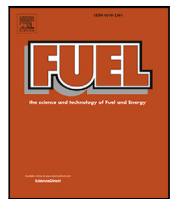
Citation (APA):
Zhang, M., Ong, J. C., Pang, K. M., Bai, X-S., & Walther, J. H. (2022). Effects of ambient CO₂ and H₂O on soot processes in n-dodecane spray combustion using large eddy simulation. *Fuel*, 312, Article 122700. <https://doi.org/10.1016/j.fuel.2021.122700>

General rights

Copyright and moral rights for the publications made accessible in the public portal are retained by the authors and/or other copyright owners and it is a condition of accessing publications that users recognise and abide by the legal requirements associated with these rights.

- Users may download and print one copy of any publication from the public portal for the purpose of private study or research.
- You may not further distribute the material or use it for any profit-making activity or commercial gain
- You may freely distribute the URL identifying the publication in the public portal

If you believe that this document breaches copyright please contact us providing details, and we will remove access to the work immediately and investigate your claim.



Full length article

Effects of ambient CO₂ and H₂O on soot processes in *n*-dodecane spray combustion using large eddy simulationMin Zhang ^a, Jiun Cai Ong ^{a,*}, Kar Mun Pang ^b, Xue-Song Bai ^c, Jens H. Walther ^{a,d}^a Department of Mechanical Engineering, Technical University of Denmark, 2800 Kgs. Lyngby, Denmark^b MAN Energy Solutions, Teglholmsgade 41, 2450 Copenhagen, Denmark^c Division of Fluid Mechanics, Lund University, P.O. Box 118, S-221 00 Lund, Sweden^d Computational Science and Engineering Laboratory, ETH Zürich, CH-8092 Zürich, Switzerland

ARTICLE INFO

Keywords:

Spray A
Soot processes
CO₂ addition
H₂O addition
LES

ABSTRACT

In this study, large eddy simulations, coupled a two-equation soot model, are performed to investigate the effects of ambient carbon dioxide (CO₂) and water (H₂O) additions on the soot formation and oxidation processes in an *n*-dodecane spray flame. In the soot model, acetylene (C₂H₂) is soot precursor and surface growth species, while hydroxyl radical (OH) and oxygen (O₂) are soot oxidizers. The effect of ambient CO₂ and H₂O additions on soot formation/oxidation can be separated into thermal and chemical effects. For the thermal effects, the ambient CO₂ and H₂O additions increase C₂H₂ but reduce OH formation by lowering the flame temperature. This leads to a higher soot mass formed. On the contrary to the thermal effects, the ambient CO₂ and H₂O additions reduce the soot formation due to their chemical effects. The reaction CH₂^{*} + CO₂ ↔ CH₂O + CO is found to be responsible for reducing C₂H₂ formation. The ambient H₂O addition results in a higher OH but lower the C₂H₂ mass formed owing to the reverse reactions H₂ + OH ↔ H₂O + H and OH + OH ↔ H₂O + O. Furthermore, the chemical effects is more significant than the thermal effects under the tested conditions. This leads to a lower soot mass formed when adding ambient CO₂ and H₂O.

1. Introduction

Exhaust gas recirculation (EGR) has been developed to reduce the nitrogen oxides in diesel engines for the last decades [1,2]. Recent researches have shown that the components of EGR, i.e., carbon dioxide (CO₂) and water (H₂O), have significant influence on the soot formation processes [3,4]. Hence, it is fundamentally and practically important to further understand the effects of these EGR components on soot formation processes.

A great number of studies have been carried out to investigate the effect of ambient CO₂ on soot formation [5–12]. Oh et al. [4] experimentally observed that the ambient CO₂ addition leads to a reduction of the soot volume fraction (SVF) and soot particle size in a co-flow diffusion flame. A numerical study with respect to the effects of ambient CO₂ addition on the soot formation in a ethylene (C₂H₄) diffusion flame was conducted by Guo et al. [6], in which they proposed that the soot suppression effects due to the ambient CO₂ addition is mainly attributed by three mechanisms: dilution, thermal, and chemical. There has been a consensus that these three mechanisms are responsible for the effects of ambient CO₂ addition on soot formation processes [4,5, 13,14]. However, debates on the nature of the effects of ambient CO₂

addition on soot suppression still exist. Liu et al. [5] and Guo et al. [6] found that the underlying mechanism behind the soot reducing by the ambient CO₂ addition is through inhibiting the soot inception and surface growth rates, instead of promoting the oxidation processes in a laminar C₂H₄ diffusion flame. The primary reaction, CO₂ + H ↔ CO + OH, was shown to be responsible for the suppression of soot inception and surface growth. The addition of CO₂ consumes H radicals through this reaction. The reduction in the concentration of H radicals decreases the formation rate of active sites in hydrogen-abstraction-C₂H₂-addition (HACA) mechanism [6]. This in turn decreases the rates of polycyclic aromatic hydrocarbon (PAH), a soot precursor for inception and surface growth. Naseri et al. [11] investigated the influence of ambient CO₂ addition on the soot behavior in a premixed laminar C₂H₄ flame. Their results also showed that the ambient CO₂ addition reduces the soot inception and surface growth rates by lowering the concentrations of H radicals, acetylene (C₂H₂) and PAH. The sensitivity analysis suggested that the decrease in concentrations of these species stems from the reaction, CO₂ + CH₂^{*} ↔ CH₂O + CO, where CH₂^{*} is the activated methylene. On the other hand, Mc Clintock et al. [15] found that the soot suppression by the ambient CO₂ addition is due to the

* Corresponding author.

E-mail address: jcong@mek.dtu.dk (J.C. Ong).

increased soot oxidation by enhancing hydroxyl radicals (OH) concentrations. Liu et al. [8] and Tang et al. [10] carried out numerical studies of soot formation in a laminar premixed and diffusion C_2H_4 flames, in which they found that the ambient CO_2 addition inhibits the soot inception and surface growth processes by lowering the concentration of C_2H_2 , but enhances the oxidation by increasing the concentration of OH . The chemical effect of ambient CO_2 addition were attributed by the reactions $\text{CO}_2 + \text{H} \leftrightarrow \text{CO} + \text{OH}$ and $\text{CO}_2 + \text{CH} \leftrightarrow \text{CO} + \text{HCO}$.

There are a few studies reported with respect to the influence of ambient H_2O addition on soot formation processes [16–18]. Richard et al. [16] experimentally investigated the chemical and physical effects of ambient H_2O addition on soot formation in diffusion flames. They observed a decrease in the soot mass with increasing ambient H_2O addition. In the numerical study performed by Liu et al. [17] who investigated the effects of ambient H_2O addition on soot formation in a laminar C_2H_4 diffusion flame, the SVF was found to decrease with the ambient H_2O addition. They concluded that soot inception is inhibited by lowering the concentrations of H radicals and PAH. Reactions, $\text{H}_2 + \text{OH} \leftrightarrow \text{H} + \text{H}_2\text{O}$ and $\text{OH} + \text{OH} \leftrightarrow \text{O} + \text{H}_2\text{O}$, were found to be responsible for the chemical effect of ambient H_2O addition.

It should be noted that the operating conditions of the aforementioned studies were only focused on the atmospheric pressures and temperatures. However, diesel engines operate at very high temperature and pressure conditions. Patel et al. [3] experimentally investigated the effects of EGR compositions on soot formation under the Engine Combustion Network (ECN) Spray A conditions, where the ambient temperature of 900 K and pressure of 60.5 bar are used to mimic engine-like conditions. They found that the ambient CO_2 and H_2O additions suppress the soot formation and supported their findings based on the studies under the atmospheric operating conditions. Detailed information about the distribution of the soot-related species is limited as compared to experiments performed at atmospheric conditions. Hence, it is not clear whether the governing mechanisms and conclusions from those studies conducted at the atmospheric operating conditions can be projected to the engine-like conditions. Set against these backgrounds, the goal of the present study is to gain a better understanding of the mechanisms behind the soot suppression caused by the ambient CO_2 and H_2O additions under the engine-like conditions. The goal is achieved by performing large eddy simulations (LES) of Spray A with different concentrations of ambient CO_2 and H_2O at the fixed ambient temperature of 900 K and O_2 level of 15%.

The paper is organized as follows: Description of the simulated cases are provided in Section 2. The numerical methods including spray, gas phase, and soot models are described in Section 3. Validation of the model and discussion on the effects of ambient CO_2 and H_2O additions on soot formation are presented in Section 4. A concluding remark is highlighted in the last section.

2. Targeted spray setup

The present numerical studies are based on the New One Shot Engine (NOSE) setup [3], where the operating conditions corresponding to the ECN Spray A are attainable. NOSE is a rapid compression machine (RCM) with optical access, which is able to prevent the generation of preburn combustion species as in the constant volume preburn chamber (CVPC). A 4-stroke low-speed diesel engine was used and its original cylinder head was replaced by a dedicated chamber to provide a sufficient field of view and enable optical measurements from four quartz windows. The chamber is a cuboid with the volume of 240 cm³ (44 mm × 44 mm × 124 mm). The injector is mounted at the center of the chamber head. The engine is driven with a high power electric direct current motor which can achieve an accurate speed of piston movement. Detailed descriptions of the NOSE can be found in [3,19]. For brevity, the main parameters of injection conditions for the ECN Spray A are summarized here. The *n*-dodecane fuel with a temperature of 900 K and density of 713 kg/m³ is injected to the

Table 1
Ambient compositions (% mol) in the simulation cases.

Case	O_2	N_2	CO_2	XCO_2	H_2O	XH_2O
1	15	75.15	6.22	0.00	3.63	0.00
2	15	85.00	0.00	0.00	0.00	0.00
3	15	75.15	0.00	6.22	0.00	3.63
4	15	80.50	4.50	0.00	0.00	0.00
5	15	80.50	0.00	4.50	0.00	0.00
6	15	81.00	0.00	0.00	4.00	0.00
7	15	81.00	0.00	0.00	0.00	4.00

chamber through a injector nozzle with the nominal diameter of 90 μm . The injection pressure, mass flow rate, injection duration, and half of cone angle are set to 150 MPa, 2.295 g/s, 3.2 ms, and 5.5°, respectively. Seven simulations are performed at different ambient compositions at a fixed ambient temperature of 900 K and pressure of 60.5 bar are listed in Table 1. Fictitious species of XCO_2 and XH_2O are introduced for CO_2 and H_2O , respectively. These fictitious species have the same thermal properties as their chemical counterparts, but they are chemically inert. The XCO_2 and XH_2O additions affect the soot formation only through the same thermal effect resulting from the CO_2 and H_2O additions, without bringing any chemical effects. With this approach, the thermal and chemical effects on soot formation can be separated (cf. Cases 1 to 3). Furthermore, the effects of ambient CO_2 and H_2O additions on soot formation are investigated by conducting Cases 4 and 5 (CO_2 effect only) as well as Cases 6 and 7 (H_2O effect only), respectively.

3. Model framework

The simulation works are carried out using OpenFOAM-v1712 where the motion of liquid phase is modeled in a Lagrangian framework, while the gas phase flow and combustion processes are modeled in an Eulerian framework [20].

3.1. Spray model

The Lagrangian particle tracking approach is adopted to model the motion of the liquid fuel droplets. The Rosin–Rammler size distribution is adopted to describe the results from the primary break-up of droplets [21]. The maximum droplet size is restricted to the diameter of injector nozzle. The mean and minimum droplet sizes are set to 70% and 10% of the diameter of the injector nozzle, respectively [21,22]. The secondary break-up of droplets is modeled by Reitz–Diwakar model with a stripping breakup constant of 10 [23]. The Frossling model and Ranz–Marshall method are used to calculate the liquid evaporation and heat transfer between the gas and liquid phases [24,25].

3.2. Gas phase model

In the present study, the gas flow field is obtained from numerical solution of the filtered compressible Navier–Stokes equations [26,27]. The sub-grid-scale stress is modeled by a one-equation dynamic structure LES model [27]. A reduced chemical mechanism with 54 species and 269 reactions developed by Yao et al. [28] is implemented to model the pyrolysis of the *n*-dodecane fuel. The well-stirred reactor (WSR) model is implemented as the combustion model, in which the mixture is assumed to be homogeneous in each computational cell. This model has been frequently used in spray ignition simulations with acceptable accuracy [29,30]. Chishty et al. [24] compared the soot formation for *n*-dodecane spray using transported probability density function (TPDF) and WSR models under the URANS framework, in which they found that the TPDF model is shown to have limited effects on soot production. While the importance of TCI in simulating soot prediction in diesel spray flames under the LES framework needs to be evaluated [31], the LES-WSR model performs reasonably well for the current test conditions [32]. The chemistry coordinate mapping (CCM)

Table 2
The soot sub-models adopted from [32].

Physical processes [units]	Mathematical expressions
Inception [mole/(m ³ ·s)]	$\omega_{inc} = 10000 \exp\left(\frac{21000}{T}\right) [\text{C}_2\text{H}_2]$
Surface growth [mole/(m ³ ·s)]	$\omega_{sg} = 45(p/p_{ref})^{1.4} \exp\left(\frac{12100}{T}\right) S_{soot}^{0.5} [\text{C}_2\text{H}_2]$
Coagulation [1/(m ³ ·s)]	$\omega_{coag} = 3 \left(\frac{24k_B T}{\rho_{soot}}\right)^{0.5} \left(\frac{6M_{soot}}{\pi\rho_{soot}}\right)^{\frac{1}{6}} N_{soot}^{\frac{11}{6}}$
Oxidation via OH [mole/(m ³ ·s)]	$\omega_{OH} = 1.146T^{0.5} S_{soot}^{0.5} [\text{OH}]$
Oxidation via O ₂ [mole/(m ³ ·s)]	$\omega_{O_2} = 10000T^{0.5} \exp\left(\frac{19778}{T}\right) S_{soot}^{0.5} [\text{OH}]$

approach is implemented to improve the computation efficiency in integrating the source terms in the elementary reaction and energy equations. Detailed implementations and theories of CCM are available in [33–35].

3.3. Soot model

In the present study, one-way coupling between soot and gas phase is considered, which has been widely used in many studies [24,36,37]. A two-equation soot model, which considers soot inception, coagulation, surface growth as well as oxidation via OH and O₂, is incorporated into the flow solver [25] to model the soot processes. This two-equation soot model has been widely used in many studies [24,38,39]. In this model two transport equations are solved for the soot mass fraction (Y_{soot}) and soot particle number density (ϕ_N),

$$\frac{\partial}{\partial t}(\rho Y_{soot}) + \frac{\partial}{\partial x_j}(\rho u_j Y_{soot}) = \frac{\partial}{\partial x_j} \left(\frac{\mu_t}{Sc_t} \frac{\partial Y_{soot}}{\partial x_j} \right) + \frac{d M_{soot}}{dt} \quad (1)$$

$$\frac{\partial}{\partial t}(\rho \phi_N) + \frac{\partial}{\partial x_j}(\rho u_j \phi_N) = \frac{\partial}{\partial x_j} \left(\frac{\mu_t}{Sc_t} \frac{\partial \phi_N}{\partial x_j} \right) + \frac{1}{N_A} \frac{d N_{soot}}{dt} \quad (2)$$

where ρ , u_j , μ_t , and Sc_t denote the spatially filtered fluid density, flow velocity, turbulent viscosity, and turbulent Schmidt number, respectively. The laminar Schmidt number for soot particle is very high, resulting in a very small molecular diffusivity. In addition, the turbulent diffusivity is much higher than the molecular diffusivity in the spray flame. Hence, the molecular diffusion coefficient of soot particles is set to zero and only turbulent diffusivity ($\frac{\mu_t}{Sc_t}$) is considered. The turbulent Schmidt number is set to 0.7. The value of Avogadro number is $N_A = 6.022045 \times 10^{23} \text{ mol}^{-1}$.

The source terms ($\frac{d M_{soot}}{dt}$ and $\frac{d N_{soot}}{dt}$) denote the net soot mass and particle number production rates, respectively. Their expressions are written as follows,

$$\frac{d M_{soot}}{dt} = MW_c \left(100\omega_{inc} + 2\omega_{sg} - \omega_{OH} - \omega_{O_2} \right) \quad (3)$$

$$\frac{d N_{soot}}{dt} = N_A \omega_{inc} - \omega_{coag} \quad (4)$$

where MW_c is the molecular weight of carbon atom. Each incipient soot particle is assumed to contain 100 carbon atoms [40]. The first to fourth terms on the right hand of Eq. (3) represent the sub-model reaction rates of inception, surface growth as well as oxidation via OH and O₂. ω_{coag} denotes the coagulation rate of soot particles.

The formulations of all soot sub-model reaction rates are listed in Table 2. Therein, P , P_{ref} , T , and S_{soot} denote the gas pressure, atmospheric pressure, gas temperature, and soot specific surface area, respectively. It should be noted that the sub-model constants are adopted from the previous study [32]. The soot density (ρ_{soot}) and Boltzmann's constant (k_B) are 2000 kg/m³ and 1.38054×10^{-23} J/K, respectively. The SVF is calculated from Y_{soot} and is expressed as follows,

$$\text{SVF} = \frac{\rho Y_{soot}}{\rho_{soot}} \quad (5)$$

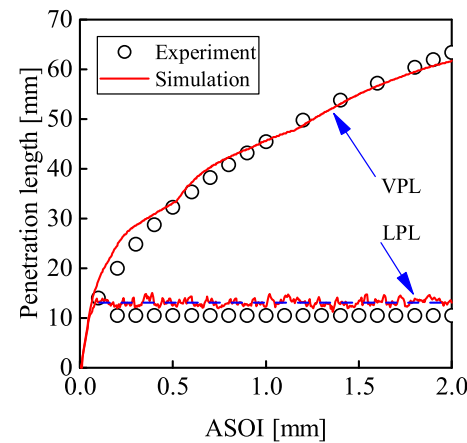


Fig. 1. Comparison of the simulated and measured liquid and vapor penetration lengths (LPL and VPL) [19] after start of injection (ASOI). Dashed line denotes the time averaged LPL from 0.1 ms to 2.0 ms.

3.4. Computational domain and numerical schemes

The computational domain is a cuboid with the volume of 0.241 liter (44 mm × 44 mm × 124 mm), corresponding to the NOSE chamber. A uniform mesh with size of 0.25 mm is implemented to cover the spray region. In order to solve the high gradient of velocity in the liquid region, a finer mesh of 0.125 mm is employed to cover the space between the nozzle and 15 mm downstream location. In addition, a coarser mesh is employed outside of the spray region. Although the chamber dimensions of the NOSE and CVPC are different, the mesh resolutions within the liquid and spray regions for the NOSE are the same as those used for the CVPC in the authors' previous study [32], where the detailed descriptions of mesh configurations and resolution sensitivity are available. The computational time step is set to 50 ns. Both time and space are discretized using second-order schemes.

4. Results and discussion

4.1. Model validations

4.1.1. Inert spray validation

The model performance is first validated by comparing the experimental and simulated non-reacting spray characteristics with a focus on liquid penetration length (LPL) and vapor penetration length (VPL). In the present study, the LPL is defined as the maximum axial distance from the nozzle to the downstream location with the liquid fuel mass reaching 95% of its total instantaneous value [41], while the VPL is defined as the axial distance from the nozzle to the downstream location where 0.1% fuel mass fraction is observed [42]. Fig. 1 shows a comparison of the measured and simulated LPLs and VPLs. It should be noted that the measured data is the quasi-steady value ensemble-averaged from 12 repeatable experimental tests [19], while the simulated data is from a single realization. As depicted in Fig. 1, both the simulated LPL and VPL show reasonable agreements with their corresponding measured values [19]. A slight difference between the measured and simulated values of LPL can be attributed to the uncertainty of liquid spreading angle (half angle) between simulation and experiment. Manin et al. [43] and Payri et al. [44] experimentally measured this angle at quasi-steady state (QSS) to be 5.5° and 10°, respectively. It is expected that the simulated LPL decreases and approaches to the measured LPL as the liquid spreading angle increases from 5.5° to 10.0°. Nevertheless, the relative error of LPL is less than 20%, when the liquid spreading angle of 5.5° is used in the present study.

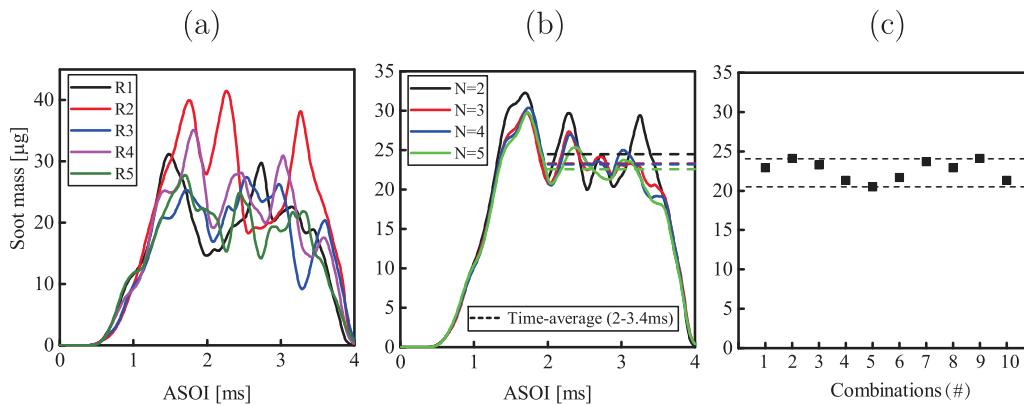


Fig. 2. Temporal evolution of (a) soot mass for the individual realizations (R1–R5) and (b) ensemble-averaged soot mass based on different number of realizations (N) in Case 1 (6.22% CO₂, 3.63% H₂O, 15% O₂, 75.15% N₂) after start of injection (ASOI). The time average of ensemble-averaged soot mass from 2.0 ms to 3.4 ms are represented by dashed lines. (c) Time average of ensemble-averaged soot mass obtained from different combinations of N = 3.

Table 3
Comparisons of the experimental [3] and simulated lift-off lengths.

Case	Experiment (mm)	Simulation (mm)
1	17.3	19.2
2	17.6	18.6
3	N/A	17.8
4	18.2	18.6
5	N/A	20.0
6	17.4	19.4
7	N/A	19.5

Note: N/A denotes that the experimental data in these cases are not available.

4.1.2. Reacting spray validation

The reacting spray characteristics in terms of ignition delay time (IDT) and lift-off length (LOL) are then assessed by comparing experimental and simulated data. In the present study, the IDT, as recommended by the ECN [41,45], is defined as the time when the maximum rate of change of the maximum temperature is observed. The LOL, as suggested by the ECN [41,46], is defined as the shortest distance from the injector nozzle to the downstream location with the OH mass fraction reaching 2% of its maximum value after the stabilization of flame. The IDT measurements for Cases 2 to 7 are not available. Hence, only the simulated IDT (0.31 ms) for Case 1 is compared against the measured IDT (0.40 ms) [19]. The relative error is within 22%. The simulated IDTs for other 6 cases vary from 0.30 ms to 0.32 ms, showing that the ambient CO₂ and H₂O additions have less influence on the IDT. A comparison of the predicted and measured LOLs are listed in Table 3. The experimental LOLs are ensemble-averaged from 10 repetitive tests [3], while the simulated LOLs are obtained by performing the time-average (0.35 ms to 3 ms) and ensemble-average from 3 different realizations. The reason for the choice of 3 realizations is presented later in Section 4.1.3. The predicted LOLs show good agreements with the experimental data in all cases [3]. Besides that, one can also see that the ambient CO₂ and H₂O additions have insignificant effects on the LOL.

4.1.3. Soot validations

The soot evolution under different ambient CO₂ and H₂O additions are assessed by comparing the measured and simulated temporal soot mass. It should be noted that only the soot within the field of view (from injector nozzle to 61 mm downstream location) is measured in the experiment [3]. Hence, the same field of view is implemented in the current LES to calculate the simulated soot mass and other species scalars. Fig. 2(a) illustrates the temporal evolution of the soot mass for the 5 individual realizations in Case 1. It is apparent that the soot mass

before 1.2 ms almost coincides with each other for different realizations. This is similar to the conclusion reported by Pei et al. [31], where they carried out different realizations only before 1.0 ms ASOI under the ECN Spray A conditions. However, the soot mass from different realizations significantly varies during the quasi-steady state (QSS). This demonstrates that one single realization may not be sufficient to compare the amount of soot mass between different cases during the QSS. Fig. 2(b) depicts the temporal evolution of ensemble-averaged soot mass based on different number of realizations (N). It is obvious that the fluctuations still exist during the QSS. Considering that the present study is focused on comparing the soot mass during the QSS, the time average of the ensemble-averaged soot mass during the QSS is used to determine the minimum realizations required in the comparison of soot mass size between different cases. As shown in Fig. 2(b), the time average of ensemble-averaged soot mass from 2.0 ms to 3.4 ms are represented by dashed lines. One can see that the time-averaged values start to converge after 3 realizations. Although the convergence is not monotonic as N = 5, the difference between N = 3 and N = 5 is rather small (around 1 μg, cf. Fig. 2(c)). Such a small difference is not expected to vary the conclusion when comparing the soot mass during the QSS between different cases. It should however be noted that the sequence of averaging 3 realizations may make a difference. Fig. 2(c) shows the time average of ensemble-averaged soot mass obtained from different combinations of N = 3 for Case 1. The maximum difference of the time average of ensemble-averaged soot mass is around 3 μg, which is smaller than the soot reduction due to the thermal/chemical effects of H₂O/CO₂ additions by at least a factor of 2 (cf. Sections 4.2 and 4.3). In other words, the soot reduction is not due to the uncertainties from different combinations of N = 3. Furthermore, the main purpose of the present study is to find out the mechanisms which are responsible for the soot reduction instead of quantifying the magnitude of soot reduction due to H₂O and CO₂ additions. Therefore, the use of 3 different realizations for the subsequent ensemble-averaged calculations is deemed sufficient.

Fig. 3 compares the temporal evolution of the ensemble-averaged simulated and measured soot mass in Cases 1, 4, and 6. Both measured and simulated results of Case 2 where there is no ambient CO₂ and H₂O are also included in each sub-figure for comparison. It should be noted that the experimental results are ensemble averaged from ten different realizations, whereas the simulation results are ensemble-averaged from 3 different realizations. Although the predicted soot mass drop due to the ambient CO₂ and H₂O additions is less than that in the experiments, the current LES model coupled with the reduced n-dodecane mechanism and two-equation soot model is able to capture the soot suppression effect due to both the ambient CO₂ and H₂O additions. In addition to the soot evolution, it is also important to examine the soot distribution. Fig. 4 shows a comparison of measured

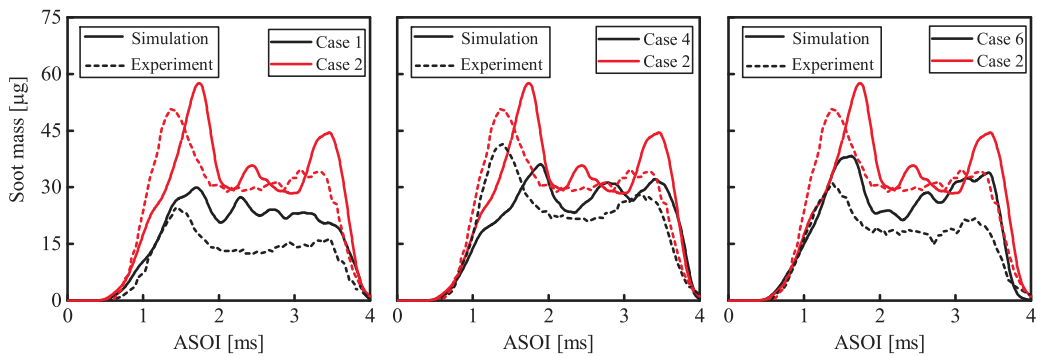


Fig. 3. Comparison of temporal evolution of the ensemble-averaged simulated and measured soot mass for Case 1 (6.22% CO₂, 3.63% H₂O, 15% O₂, 75.15% N₂), Case 2 (0% CO₂, 0% H₂O, 15% O₂, 85% N₂), Case 4 (4.50% CO₂, 0% H₂O, 15% O₂, 80.5% N₂) and Case 6 (0% CO₂, 4% H₂O, 15% O₂, 81% N₂) after start of injection (ASOI).

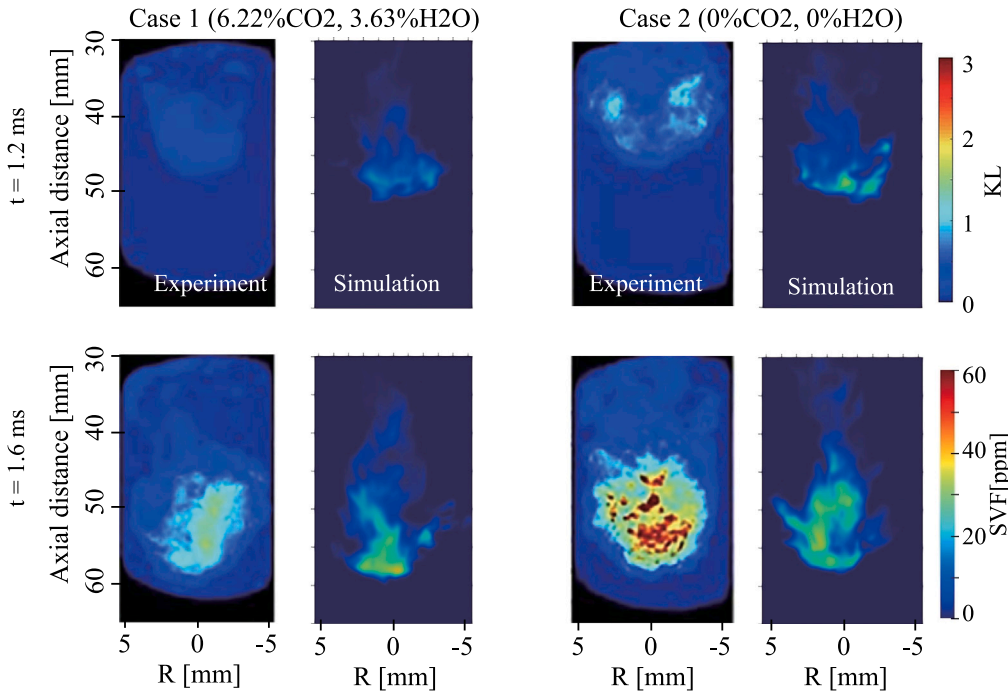


Fig. 4. Comparison of the temporal evolution of the measured soot optical thickness (KL) and simulated soot volume fraction (SVF) at two different time instances (1.2 ms and 1.60 ms) for Case 1 (6.22% CO₂, 3.63% H₂O, 15% O₂, 75.15% N₂) and Case 2 (0% CO₂, 0% H₂O, 15% O₂, 85% N₂).

soot optical thickness (KL) and simulated SVF for Cases 1 and 2 at two different time instances (1.2 ms and 1.6 ms). The realization numbers used for the ensemble average are the same as that used in Fig. 2. As shown in Fig. 4, the penetration of SVF and the evolution of soot-containing regions are well captured by the present LES model. Overall, Figs. 3 and 4 collectively demonstrate that the present model is able to capture the soot formation process well under different ambient compositions.

4.2. Thermal effects

As mentioned earlier, the effects of ambient CO₂ and H₂O additions on soot formation is mainly due to dilution, thermal, and chemical mechanisms [6,13,14]. Since the ambient O₂ level is fixed at 15% on molar basis for different cases, the dilution effect can be disregarded. Fig. 5 shows a comparison of temporal evolution of the ensemble-averaged soot mass for Case 1 (6.22% CO₂, 3.63% H₂O, 15% O₂, 75.15% N₂), Case 2 (0% CO₂, 0% H₂O, 15% O₂, 85% N₂), and Case 3 (6.22% XCO₂, 3.63% XH₂O, 15% O₂, 75.15% N₂). The dashed lines represent the time-averaged soot mass from 2.0 ms to 3.4 ms. It is

apparent that the soot formation is affected by both the thermal and chemical effects. The results does not agree with the findings in [11], where the thermal effect only has minor influence on the soot formation in a premixed laminar flame under atmospheric condition. Hence, it is suggested that the thermal effects on soot formation become more significant under the engine-like conditions. As shown in Fig. 5, the soot mass is promoted by the thermal effect instead of being suppressed. Since the ambient CO₂ and H₂O have the similar thermal properties, their thermal effects on soot formation are expected to be similar. Therefore, the combined thermal effects of ambient CO₂ and H₂O additions on soot formation is studied in this section. The chemical effects of ambient CO₂ and H₂O will then be discussed in Section 4.3.

To further understand the thermal effects of ambient CO₂ and H₂O additions, the mean flame temperatures in Cases 2 and 3 as function of the equivalence ratio (ψ) at 2.5 ms ASOI are shown in Fig. 6. It should be noted that only the cells with the flame temperature greater than 1400 K are considered. One can see that the mean flame temperature at the fuel-rich side in Case 2 is higher than that in Case 3. Similar finding can be observed at other time instances after the flame stabilizes. The

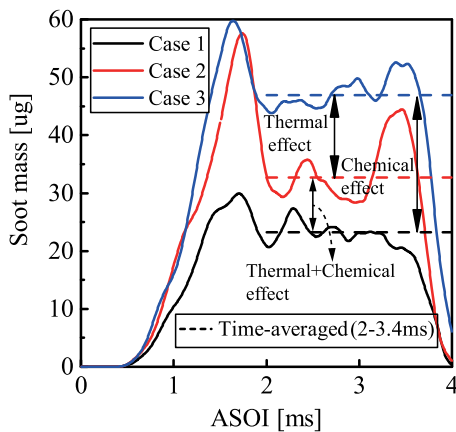


Fig. 5. Comparison of temporal ensemble-averaged soot mass evolution in Case 1 (6.22% CO₂, 3.63% H₂O, 15% O₂, 75.15% N₂), Case 2 (0% CO₂, 0% H₂O, 15% O₂, 85% N₂), and Case 3 (6.22% XCO₂, 3.63% XH₂O, 15% O₂, 75.15% N₂) after start of injection (ASOI).

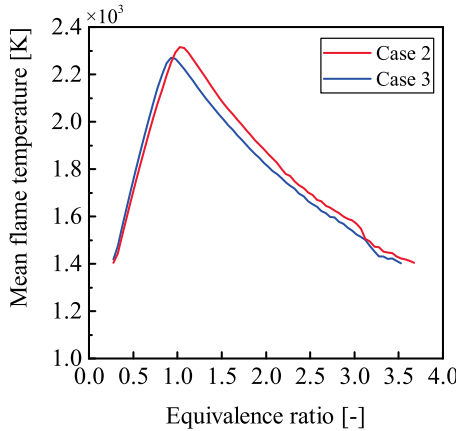


Fig. 6. Comparison of mean flame temperature as function of equivalence ratio between Case 2 (0% CO₂, 0% H₂O, 15% O₂, 85% N₂) and Case 3 (6.22% XCO₂, 3.63% XH₂O, 15% O₂, 75.15% N₂) at 1.0 ms after start of injection (ASOI).

higher mean flame temperature in Case 2 can be attributed to the fact that CO₂ and H₂O have a higher heat capacity than N₂. Despite having a higher flame temperature, Fig. 5 shows that the soot mass in Case 2 is lower than that in Case 3. Hence, the difference in flame temperature resulted from the thermal effect is not the direct reason for the difference in the soot mass between Cases 2 and 3.

Considering that the soot formation is highly dependent on the soot-related species, the temporal evolution of the ensemble-averaged C₂H₂ and OH mass are provided in Fig. 7. As depicted, the C₂H₂ mass starts to differ after 1.0 ms ASOI, while the OH mass starts to differ after ignition has occurred. It is important to note that the C₂H₂ mass is higher, while the OH mass is lower in Case 3 as compared to Case 2, implying that the thermal properties of ambient CO₂ and H₂O additions result in a higher C₂H₂ mass but a lower OH mass. It is apparent that the higher C₂H₂ mass promotes the soot formation process and the lower OH mass decreases the soot oxidation in Case 3. Hence, a higher soot mass is observed in Case 3 (cf. Fig. 5). Since air-fuel mixing is important to the formation of C₂H₂ and OH, the air entrainment may be another factor which varies the C₂H₂ and OH production upon ambient CO₂ and H₂O additions. Yet, as shown earlier in Table 3, the mean LOLs in Case 2 and 3 are similar. This indicates a similar air entrainment in the two flames. To confirm this, the temporal evolution of the total mass of air entrainment is examined in Appendix B.

Table 4

Initial conditions of 0-D homogeneous reactor for Case 2.

Initial conditions	Values
Pressure (bar)	60.5
CO ₂ /XCO ₂ (mol %)	0/0
H ₂ O/XH ₂ O (mol %)	0/0
O ₂ /N ₂ (mol %)	15/85
ψ/T ([·]/K)	1.0/832, 1.5/805, 2.0/780

Note: ψ and T denote equivalence ratio and initial temperature, respectively.

It should be noted that a higher flame temperature in Case 2 is predicted, as shown in Fig. 6. Generally, a higher flame temperature results in a higher production of OH [47,48]. To better understand the effects of temperature on C₂H₂ formation, an examination of C₂H₂ production rate is carried out by performing a 0-D homogeneous reactor simulation using ANSYS Chemkin-Pro [49]. The 0-D reactor is assumed to be adiabatic and closed with constrained pressure. The initial conditions of 0-D homogeneous reactor for Case 2 are listed in Table 4. Three different equivalence ratios ($\psi = 1.0, 1.5$, and 2.0) are simulated. The initial temperatures for these three different ψ , sampled along the adiabatic mixing line, are 832 K, 805 K, and 780 K, respectively (Details of adiabatic mixing line can be found in Appendix A). The results indicate that the two most important pathways for the C₂H₂ oxidization are



and



Fig. 8 shows the temporal evolution of O radical mass in Cases 2 and 3. It is apparent that the O radical mass in Case 2 is higher than that in Case 3 due to its higher flame temperature. These higher O and OH radicals mass in Case 2 collectively leads to a stronger oxidation of C₂H₂. Hence, a lower C₂H₂ mass and soot production during the QSS is observed in Case 2.

4.3. Chemical effects

Since the responsible reactions for the chemical effects of CO₂ and H₂O on soot formation are different, the effects of CO₂ and H₂O are investigated individually in this section.

4.3.1. Effects of ambient CO₂ on soot processes

The chemical effects of ambient CO₂ additions are investigated by comparing Case 4 (4.50% CO₂, 0% H₂O, 15% O₂, 80.50% N₂) and Case 5 (4.50% XCO₂, 0% H₂O, 15% O₂, 80.50% N₂). Fig. 9 shows a comparison of temporal evolution of the ensemble-averaged soot mass between Cases 4 and 5. A lower soot mass observed in Case 4 demonstrates that the soot formation is suppressed by the chemical effect of ambient CO₂ addition. The flame temperatures in Cases 4 and 5 are similar (not shown) as the flame temperature is only a function of the thermal properties of CO₂ instead of its chemical reactions [11]. Hence, the flame temperature is not the reason for the difference in the soot mass during the QSS between Cases 4 and 5. As claimed earlier, the similar LOLs (cf. Table 3) also cannot result in the change of soot mass between Cases 4 and 5. The difference in the soot mass between Cases 4 and 5 is likely due to the different C₂H₂ and OH concentrations. Fig. 10 compares the temporal evolution of the ensemble-averaged C₂H₂ and OH mass in Cases 4 and 5, respectively. It is apparent that the C₂H₂ mass is lower but the OH mass is slightly higher in Case 4, as compared to Case 5. Hence, the suppression of C₂H₂ is the main reason to result in a lower soot mass in Case 4.

In premixed laminar C₂H₄ flames, the suppression of soot mass due to the ambient CO₂ addition is mainly through suppressing the soot

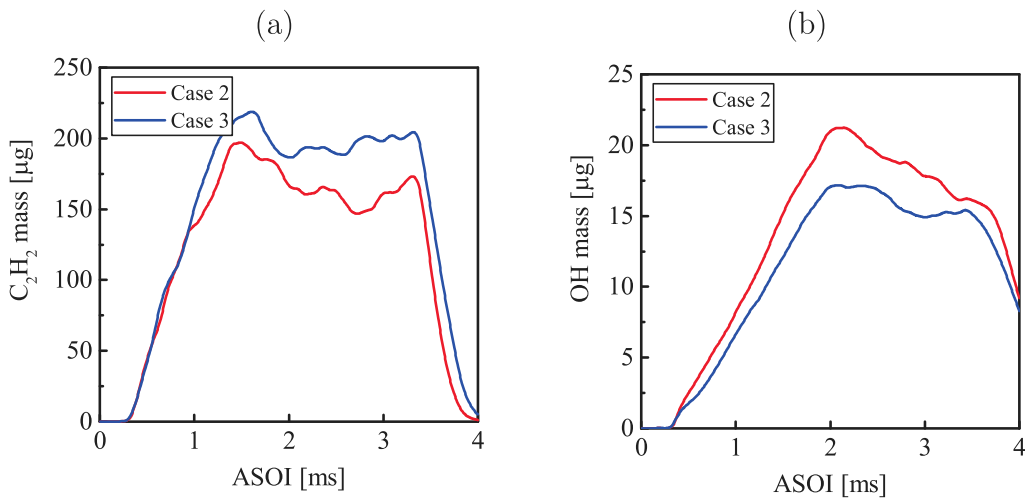


Fig. 7. Comparison of temporal evolution of the ensemble-averaged (a) C_2H_2 and (b) OH mass between Case 2 (0% CO_2 , 0% H_2O , 15% O_2 , 85% N_2) and Case 3 (6.22% XCO_2 , 3.63% XH_2O , 15% O_2 , 75.15% N_2) after start of injection (ASOI).

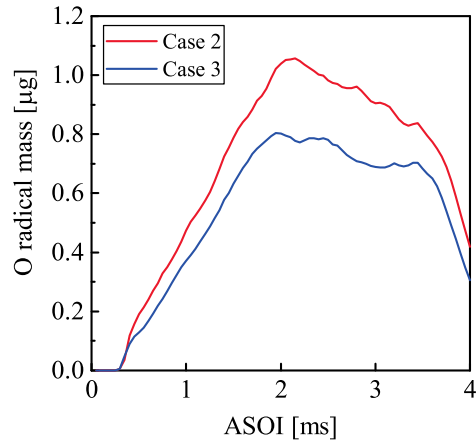


Fig. 8. Comparison of temporal evolution of the ensemble-averaged O radical mass between Case 2 (0% CO_2 , 0% H_2O , 15% O_2 , 85% N_2) and Case 3 (6.22% XCO_2 , 3.63% XH_2O , 15% O_2 , 75.15% N_2) after start of injection (ASOI).

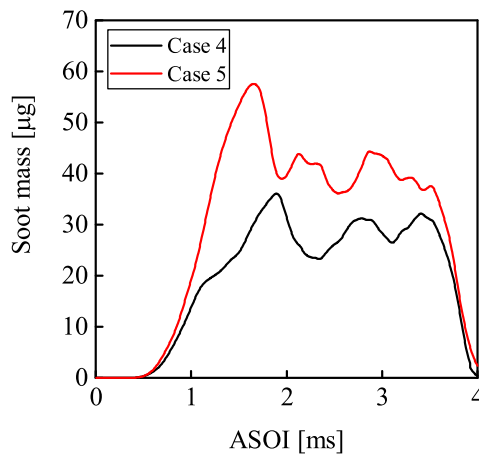


Fig. 9. Comparison of temporal evolution of the ensemble-averaged soot mass between Case 4 (4.50% CO_2 , 0% H_2O , 15% O_2 , 80.50% N_2) and Case 5 (4.50% XCO_2 , 0% H_2O , 15% O_2 , 80.50% N_2) after start of injection (ASOI).

formation but not enhancing oxidation rates [10]. On the contrary, for co-flow diffusion C_2H_2 flames the suppression on the soot mass

Table 5
Initial conditions of 0-D homogeneous reactor for cases 4 and 5.

Initial conditions	Case 4	Case 5
Pressure (bar)	60.5	60.5
CO_2/XCO_2 (mol %)	4.5/0.0	0.0/4.5
H_2O/XH_2O (mol %)	0.0/0.0	0.0/0.0
O_2/N_2 (mol %)	15.0/80.5	15.0/80.5
ψ/T ([·]/K)	1.0/832, 1.5/805, 2.0/780	

Note: ψ and T denote equivalence ratio and initial temperature, respectively.

is through both inhibiting the soot formation and enhancing the soot oxidation [5,6]. Although the mechanisms for the soot suppression due to the chemical effects of ambient CO_2 addition are different, the same responsible chemical reaction,



has been reported in these studies. When only considering this reaction, the addition of ambient CO_2 is likely to promote the OH formation in Case 4, as shown in Fig. 10(a). It should be noted that the deviation of OH mass occurs after 2 ms ASOI, while the soot mass deviates at 1 ms ASOI (cf. Fig. 9). Therefore, reaction (R3) may not be the governing chemical reaction for the chemical effect of ambient CO_2 addition. As shown in Fig. 10(b), the difference in the C_2H_2 mass is more significant than that in the OH mass as the ambient CO_2 is added. In addition, the deviation of C_2H_2 occurs after 1 ms ASOI, which corresponds to the deviation time in the soot mass (cf. Fig. 9). Hence, it is necessary to further investigate how the chemical effects of ambient CO_2 addition suppress the formation of C_2H_2 . In order to understand this, a reaction sensitivity analysis of C_2H_2 for Cases 4 and 5 is carried out.

The reaction sensitivity analysis is used to track the most influential reactions for a specific specie. The positive sensitivity coefficient indicates that an increase in the forward reaction rate increases the C_2H_2 concentration, thereby promoting reactivity. On the contrary, a negative sensitivity coefficient indicates a decrease in C_2H_2 concentration. The reaction sensitivity analysis is obtained by performing a 0-D homogeneous reactor where the initial conditions of 0-D homogeneous reactor for Cases 4 and 5 are listed in Table 5. Three different ψ -value ($\psi = 1.0, 1.5$, and 2.0) are simulated. The initial temperatures for these three ψ -value, sampled along the adiabatic mixing line, are 832 K, 805 K, and 780 K, respectively. When the $\psi = 1.0$ and 2.0 , the sensitivity analysis results do not show the reactions containing species CO_2 among the top 20 reactions. This is likely due to only a few amount C_2H_2 formed at $\psi = 1.0$ and 2.0 . Based on our simulation

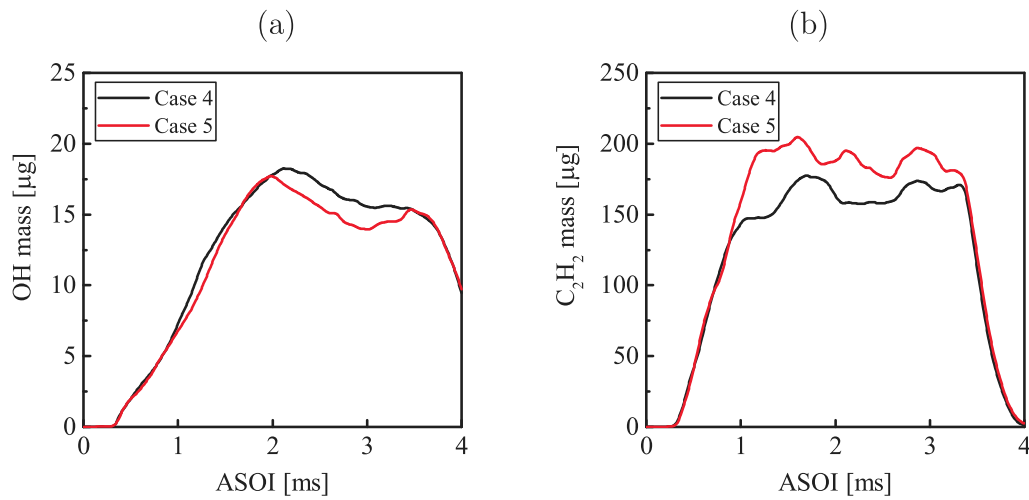


Fig. 10. Comparison of temporal evolution of the ensemble averaged (a) OH and (b) C₂H₂ mass between Case 4 (4.50% CO₂, 0% H₂O, 15% O₂, 80.50% N₂) and Case 5 (4.50% XCO₂, 0% H₂O, 15% O₂, 80.50% N₂) after start of injection (ASOI).

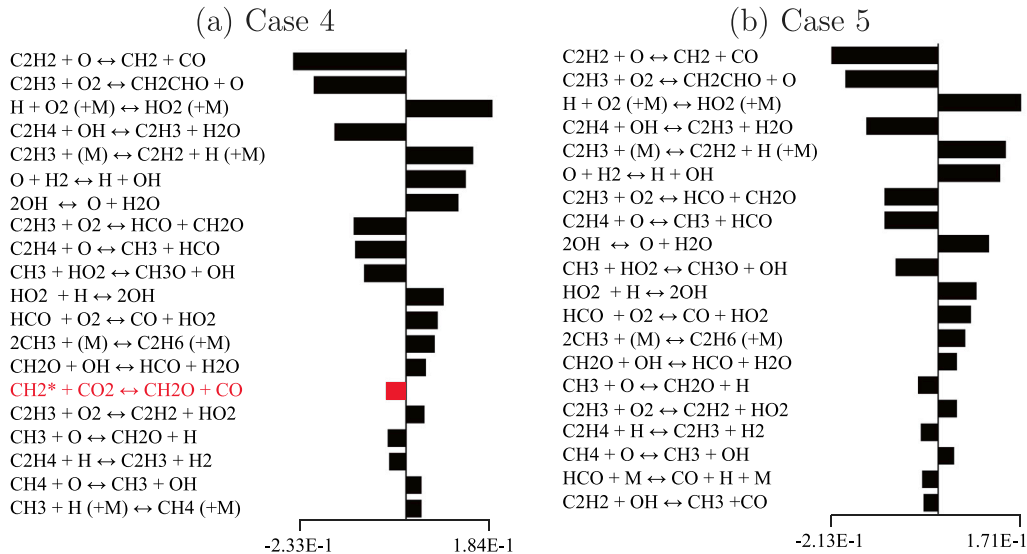


Fig. 11. Comparison of sensitivity analysis of C₂H₂ between Case 4 (4.50% CO₂, 0% H₂O, 15% O₂, 80.50% N₂) and Case 5 (4.50% XCO₂, 0% H₂O, 15% O₂, 80.50% N₂) at $\psi = 1.5$.

results (not shown here), the $\psi = 1.5$ is the most favorable region for soot formation. Hence, only the comparison of reaction sensitivity analysis of C₂H₂ between Cases 4 and 5 at $\psi = 1.5$ is shown in Fig. 11. The reaction (R3), which was proposed to be governing the soot suppression under the atmospheric conditions in many studies [5,6,8–10], is not important in the present engine-like conditions, as it is not shown among the top 20 reactions in Fig. 11. Instead, the reaction



appears upon the addition of ambient CO₂. This reaction does not appear to be significant in Case 5. CH₂^{*} is the activated methylene. It is worth noting that Naseri et al. [11] also pointed out the important influence of reaction (R4) on C₂H₂ and C₆H₆ in a premixed flame under atmospheric conditions. The direct relation between this reaction and C₂H₂ formation cannot be found. However, it should be noted that the addition of ambient CO₂ depletes CH₂^{*} which is an important source of CH₂ by the following reaction,



where M is the third-body. This leads to less CH₂ formed in Case 4, which is further confirmed by a comparison of CH₂ between Cases 4

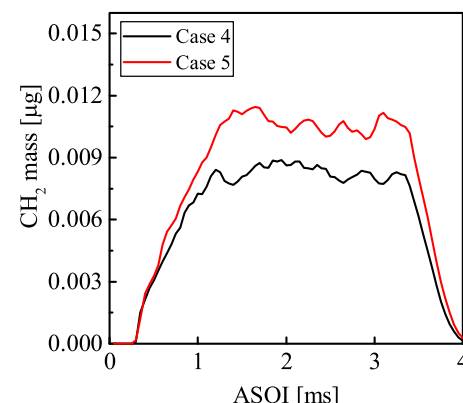


Fig. 12. Comparison of temporal evolution of the ensemble-averaged CH₂ between Case 4 (4.50% CO₂, 0% H₂O, 15% O₂, 80.50% N₂) and Case 5 (4.50% XCO₂, 0% H₂O, 15% O₂, 80.50% N₂) after start of injection (ASOI).

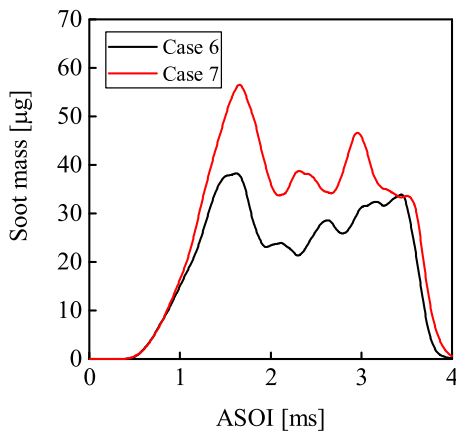


Fig. 13. Comparison of temporal evolution of the ensemble-averaged soot mass between Case 6 (0% CO₂, 4% H₂O, 15% O₂, 81% N₂) and Case 7 (0% XCO₂, 4% XH₂O, 15% O₂, 81% N₂) after start of injection (ASOI).

Table 6
Initial conditions of 0-D homogeneous reactor for cases 6 and 7.

Initial conditions	Case 4	Case 5
Pressure (bar)	60.5	60.5
CO ₂ /XCO ₂ (mol %)	0.0/0.0	0.0/0.0
H ₂ O/XH ₂ O (mol %)	4.0/0.0	0.0/4.0
O ₂ /N ₂ (mol %)	15.0/81.0	15.0/81.0
ψ/T ([J]/K)	0.8/844, 1.0/832, 1.2/821	

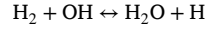
Note: ψ and T denote equivalence ratio and initial temperature, respectively.

and 5 in Fig. 12. As mentioned earlier, the reaction (R1) is one of the most important reactions to C₂H₂ oxidation. Consequently, a lower CH₂ in Case 4 leads to more C₂H₂ consumed by reaction (R1), resulting in a lower C₂H₂ in Case 4.

4.3.2. Effects of ambient H₂O on soot processes

In this section, the chemical effects of H₂O additions are investigated by comparing Case 6 (0% CO₂, 4% H₂O, 15% O₂, 81% N₂) and Case 7 (0% XCO₂, 4% XH₂O, 15% O₂, 81% N₂). Fig. 13 shows a comparison of ensemble-averaged soot evolution between Cases 6 and 7. It is apparent that the soot mass in Case 6 is lower than that in Case 7. The flame temperature profiles and LOLs are similar in Cases 6 and 7. As claimed earlier in Section 4.3.1, these are not the reason for the difference in the soot mass after the ambient H₂O is added. Fig. 14 shows a comparison of evolution of the ensemble-averaged C₂H₂ and OH mass between Cases 6 and 7. One can see that the C₂H₂ mass in Case 6 is lower than that in Case 7. This leads to a lower soot formation in Case 6. Conversely, the OH mass in Case 6 is higher, resulting in a stronger oxidation on soot, as compared to Case 7. These collectively lead to a lower soot mass formed in Case 6.

The chemical effects of ambient H₂O addition on C₂H₂ and OH production are next examined. In the present study, a 0-D homogeneous reactor simulation of OH production rates is carried out. The initial conditions of 0-D homogeneous reactor for Cases 6 and 7 are listed in Table 6. Considering that the most OH is formed around stoichiometric mixture fraction ($\psi = 1.0$), three different ψ -value ($\psi = 0.8, 1.0$, and 1.2) are simulated. The initial temperatures for these three different ψ -value, sampled along the adiabatic mixing line, are 844 K, 832 K, and 821 K, respectively. The results show that the reaction (R6) is the most important reaction to affect OH production in all the reactions including species H₂O at $\psi = 0.8$ and 1.0, while the reaction (R7) is important at $\psi = 1.2$.



The reverse reaction of (R7) becomes an important source of OH formation when ambient H₂O is added, as speculated by Richard et al. [16] where they experimentally investigated the chemical effects of ambient H₂O addition in a diffusion flame under atmospheric conditions. In addition, Liu et al. [17] also found that the reverse reactions of (R6) and (R7) are the primary pathways for the chemical effects of ambient H₂O addition under atmospheric conditions. As a result, the reactions (R6) and (R7) are found to be governing the chemical effects of ambient H₂O addition under both the engine-like and atmospheric conditions.

To further investigate how these two reactions play the role in Cases 6 and 7, a comparison of OH production rates resulting from the reactions (R6) and (R7) in the 0-D analysis of Cases 6 and 7 at $\psi = 0.8, 1.0$, and 1.2 is shown in Fig. 15. The OH productions start earlier in Case 6 due to the ambient H₂O additions. The shifted Case 7 represented by dashed line is used to facilitate the comparison of the OH production rates between Cases 6 and 7. From Fig. 15(a) and (b), the OH production rates from the reverse reaction of (R6) during the ramp-up process (indicated by black arrows) are higher in Case 6 than that in Case 7, resulting in a higher OH mass production in Case 6. In Fig. 15(c), one can see that the OH consumption rate from the forward reaction of (R7) in Case 6 is lower than that in Case 7 as the ambient H₂O additions enhance the reverse reaction of (R7). This leads to less OH consumed and thus more OH mass observed in Case 6 (cf. Fig. 14(b)). As mentioned earlier, OH is one of the most important oxidizers. Hence, a higher OH mass in Case 6 leads to a higher C₂H₂ oxidation via the reactions (R2), resulting in a lower C₂H₂ mass and thus soot surface growth rate. Meanwhile, the higher OH mass enhances the soot oxidation. Hence, these collectively result in the soot mass decreasing when adding ambient H₂O in Case 6.

5. Conclusions

In this study, the effects of ambient carbon dioxide (CO₂) and water (H₂O) additions on the soot formation are investigated using large eddy simulation at the ambient temperature of 900 K, pressure of 60.5 bar, and oxygen level of 15%. A two-equation soot model is implemented to model soot formation/oxidation process, in which acetylene (C₂H₂) is selected as soot precursor and surface growth species while hydroxyl radicals (OH) and oxygen (O₂) are soot oxidizers. The non-reacting and reacting spray characteristics in terms of liquid and vapor penetration lengths, ignition delay time, lift-off length, and soot distributions show good agreement with the experimental data. In order to compare the soot mass at the quasi-steady state (QSS) between different cases, a time-average of the ensemble-averaged soot mass is carried out. A minimum of 3 realizations are found to be sufficient to compare the soot mass size during the QSS between different cases.

It should be noted that the ambient CO₂ and H₂O additions influence the soot formation via thermal and chemical effects. The thermal effects result from the thermal properties of CO₂ and H₂O additions. The flame temperature becomes lower after the ambient CO₂ and H₂O are added due to their higher heat capacities, as compared to nitrogen (N₂). The lower flame temperature increases the C₂H₂ formation but decreases the OH formation rates. This promotes the soot formation process. On the contrary, the chemical effects of ambient CO₂ additions decrease soot mass mainly via lowering the C₂H₂ formation. In order to understand the underlying mechanism of the influence of the ambient CO₂ addition on the C₂H₂ formation, a sensitivity analysis of C₂H₂ is performed. The results suggest that the suppression of C₂H₂ due to the ambient CO₂ addition stems from the reaction CH₂* + CO₂ ↔ CH₂O + CO, which in turn leads to a lower C₂H₂ production in the reverse reaction of C₂H₂ + O ↔ CO + CH₂. The ambient H₂O addition suppresses soot mass through lowering the C₂H₂ production but enhancing OH formation. An examination of OH production rates from a 0-D analysis

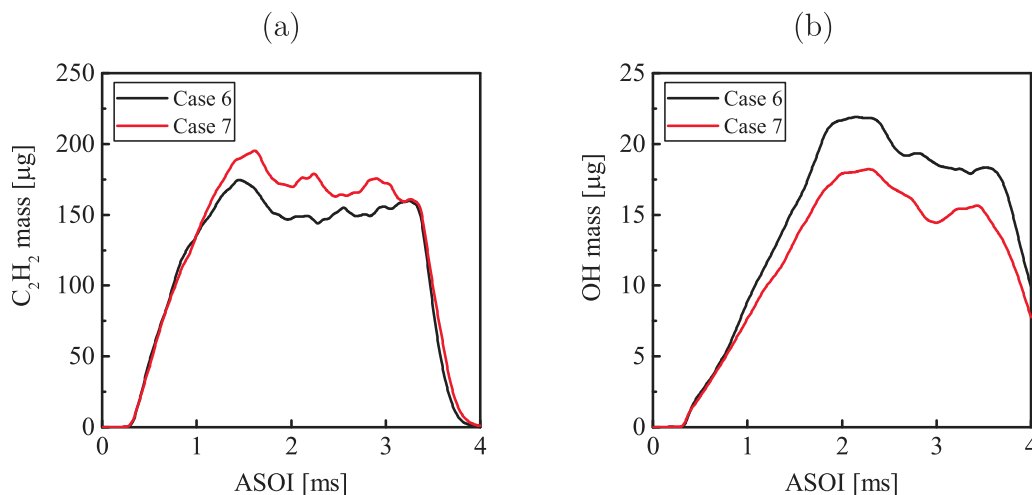


Fig. 14. Comparison of temporal evolution of the ensemble-averaged (a) C_2H_2 and (b) OH mass between Case 6 (0% CO_2 , 4.00% H_2O , 15% O_2 , 81% N_2) and Case 7 (0% XCO_2 , 4.00% XH_2O , 15% O_2 , 81% N_2) after start of injection (ASOI).

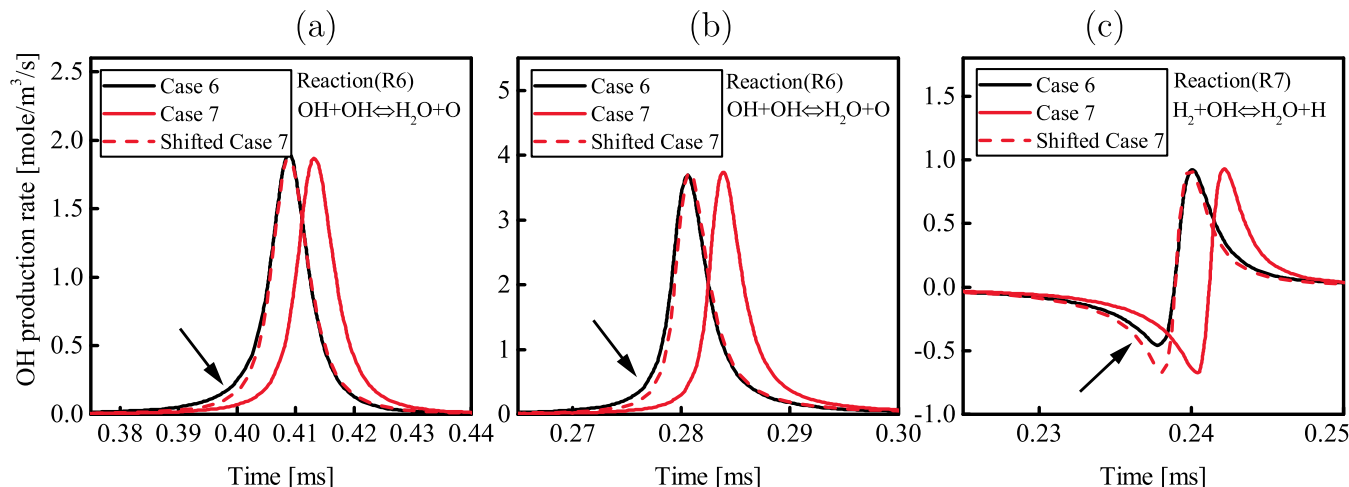


Fig. 15. Comparison of OH production rates from the reactions (R6) ($OH + OH \leftrightarrow H_2O + O$) and (R7) ($H_2 + OH \leftrightarrow H_2O + H$) in Case 6 (0% CO_2 , 4% H_2O , 15% O_2 , 81% N_2) and Case 7 (0% XCO_2 , 4% XH_2O , 15% O_2 , 81% N_2) at (a) $\gamma = 0.8$, (b) $\gamma = 1.0$, and (c) $\gamma = 1.2$.

demonstrates that the reverse reaction $H_2 + OH \leftrightarrow H_2O + H$ governs the increase in OH production and the reverse reaction of $OH + OH \leftrightarrow H_2O + O$ dominates the decrease in OH consumption rate. The increase in the OH concentration leads to a higher C_2H_2 oxidation, yielding a lower C_2H_2 and soot production. Meanwhile, the increase in OH concentration also promotes the soot oxidation, which contributes to the reduction of soot mass as well.

The present work identified the mechanisms that govern the soot suppression due to the ambient CO_2 and H_2O additions. However, it should be noted that the present work is only focused on a single ambient condition (ambient temperature of 900 K, O_2 level of 15%, and pressure of 60.5 bar). It is of high interest to expand on the current work by investigating the effect of CO_2 and H_2O on soot reduction at different ambient conditions.

CRediT authorship contribution statement

Min Zhang: Conceptualization, Methodology, Validation, Writing – original draft. **Jiun Cai Ong:** Methodology, Supervision, Writing – review & editing. **Kar Mun Pang:** Conceptualization, Supervision, Writing – review & editing. **Xue-Song Bai:** Supervision, Writing – review & editing. **Jens H. Walther:** Supervision, Writing – review & editing.

Declaration of competing interest

The authors declare that they have no known competing financial interests or personal relationships that could have appeared to influence the work reported in this paper.

Acknowledgment

Min Zhang was sponsored by China Scholarship Council (CSC). Jiun Cai Ong gratefully acknowledged the financial support from the Independent Research Fund Denmark (DFF) and MAN Energy Solutions under the grant number 8022-00143B. The computation was performed using Niflheim cluster at Technical University of Denmark (DTU). The authors acknowledged PRACE for awarding us access to Joliot-Curie at GENCI@CEA, France.

Appendix A. Adiabatic mixing line

Fig. A.1 shows scatter plot of temperature-equivalence ratio ($T - \gamma$) at 1 ms for the non-reacting case. The adiabatic mixing line is represented by the red line and obtained from [50], in which the simulation of one-dimensional counterflow diffusion flame configuration was performed using CHEM1D with the chemistry turned off to predict this line.

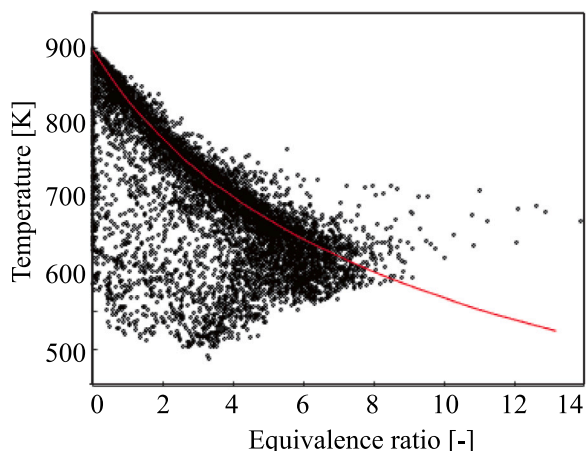


Fig. A.1. Scatter plot of temperature-equivalence ratio ($T - \psi$) at 1ms for the non-reacting case. Red line denotes the adiabatic mixing line with evaporation.

Appendix B. Examination of air entrainment in Case 2 and Case 3

The temporal evolution of mass of air entrainment between Case 2 and Case 3 is shown in Fig. B.1. The mass of air entrainment is calculated as $m_{air} = (1 - Z)m_{tot}$. m_{air} and m_{tot} are the mass of air entrainment and total vapor mass in the spray region, respectively. $Z = 0.001$ is used as a threshold to define the boundary of the spray region. As depicted, the difference in the total mass of air entrainment between Cases 2 and 3 can be disregarded. Hence, the air entrainment is not the reason to the change in C_2H_2 and OH mass when the thermal effects of ambient CO_2 and H_2O additions are introduced.

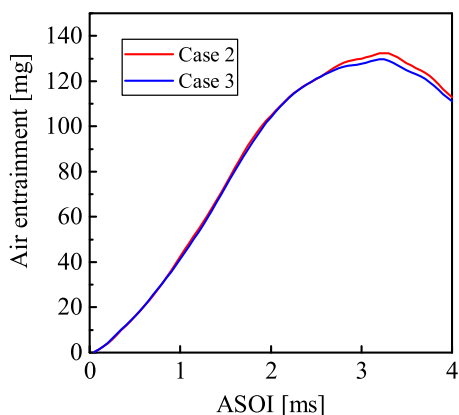


Fig. B.1. Comparison of temporal evolution of air entrainment between Case 2 (0% CO_2 , 0% H_2O , 15% O_2 , 85% N_2) and Case 3 (6.22% XCO_2 , 3.63% XH_2O , 15% O_2 , 75.15% N_2) after start of injection (ASOI).

References

- [1] Yamada H, Misawa K, Suzuki D, Tanaka K, Matsumoto J, Fujii M, Tanaka K. Detailed analysis of diesel vehicle exhaust emissions: Nitrogen oxides, hydrocarbons and particulate size distributions. *Proc Comb Inst* 2011;22:2895–902.
- [2] Kim H-M, Park S-K, Choi K-S, Wang H-M, Lee D-H, Lee D-K, Cha Y-S, Lee J-S, Lee J. Investigation on the flow and heat transfer characteristics of diesel engine EGR coolers. *Int J Automot Technol* 2008;9:149–53.
- [3] Patel C, Hespel C, Nguyen TL, Foucher F, Mounaïm-Rousselle C. Effect of exhaust gas recirculation composition on soot in ECN spray a conditions. *Oil Gas Sci Technol – Revue DIFF Energies Nouvelles* 2020;75:34.
- [4] Oh KC, Shin HD. The effect of oxygen and carbon dioxide concentration on soot formation in non-premixed flames. *Fuel* 2006;85:615–24.
- [5] Liu F, Karataş AE, Gülder ÖL, Gu M. Numerical and experimental study of the influence of CO_2 and N_2 dilution on soot formation in laminar coflow C_2H_2 /air diffusion flames at pressures between 5 and 20 atm. *Combust Flame* 2015;162:2231–47.
- [6] Guo H, Smallwood GJ. A numerical study on the influence of CO_2 addition on soot formation in an ethylene/air diffusion flame. *Combust Sci Tech* 2008;180:1695–708.
- [7] Karataş AE, Gülder ÖL. Effects of carbon dioxide and nitrogen addition on soot processes in laminar diffusion flames of ethylene-air at high pressures. *Combust Sci Tech* 2017;200:76–80.
- [8] Liu F, Guo H, Smallwood GJ, Gülder OL. The chemical effects of carbon dioxide as an additive in an ethylene diffusion flame: implications for soot and NO_x formation. *Combust Flame* 2001;125:778–87.
- [9] Mei J, You X, Law CK. Effects of CO_2 on soot formation in ethylene pyrolysis. *Combust Flame* 2020;215:28–35.
- [10] Tang Q, Mei J, You X. Effects of CO_2 addition on the evolution of particle size distribution functions in premixed ethylene flame. *Combust Flame* 2016;165:424–32.
- [11] Naseri A, Veshkini A, Thomson MJ. Detailed modeling of CO_2 addition effects on the evolution of soot particle size distribution functions in premixed laminar ethylene flames. *Combust Flame* 2017;183:75–87.
- [12] Maes N, Skeen SA, Bardi M, Fitzgerald RP, Malbec L-M, Bruneaux G, Pickett LM, Yasutomi K, Martin G. Spray penetration, combustion, and soot formation characteristics of the ECN spray C and spray D injectors in multiple combustion facilities. *Appl Thermal Engng* 2020;172:115136.
- [13] Cong TL, Dagaut P. Experimental and detailed kinetic modeling of the oxidation of methane and methane/syngas mixtures and effect of carbon dioxide addition. *Combust Sci Tech* 2008;180:2046–91.
- [14] Kailasanathan RKA, Yelverton TL, Fang T, Roberts WL. Effect of diluents on soot precursor formation and temperature in ethylene laminar diffusion flames. *Combust Flame* 2013;160:656–70.
- [15] McLintock IS. The effect of various diluents on soot production in laminar ethylene diffusion flames. *Combust Flame* 1968;12:217–25.
- [16] Richard J, Garo J, Soulé J, Vantelon J, Knorre V. Chemical and physical effects of water vapor addition on diffusion flames. *Fire Saf J* 2003;38:569–87.
- [17] Liu F, Consalvi J-L, Fuentes A. Effects of water vapor addition to the air stream on soot formation and flame properties in a laminar coflow ethylene/air diffusion flame. *Combust Flame* 2014;161:1724–34.
- [18] Teini PD, Karwat DM, Atreya A. The effect of CO_2/H_2O on the formation of soot particles in the homogeneous environment of a rapid compression facility. *Combust Flame* 2012;159:1090–9.
- [19] Nilaphai O, Hespel C, Chanchana S, Mounaïm-Rousselle C. Spray and combustion characterizations of ABE/Dodecane blend in comparison to alcohol/dodecane blends at high-pressure and high-temperature conditions. *Fuel* 2018;225:542–53.
- [20] Weller HG, Tabor G, Jasak H, Fureby C. A tensorial approach to computational continuum mechanics using object-oriented techniques. *Comput Phys* 1998;12:620–31.
- [21] D'Errico G, Lucchini T, Contino F, Jangi M, Bai X-S. Comparison of well-mixed and multiple representative interactive flamelet approaches for diesel spray combustion modelling. *Combust Theory Model* 2014;18(1):65–88.
- [22] Desantes JM, García-Olivier JM, Novella R, Pérez-Sánchez EJ. Application of a flamelet-based CFD combustion model to the LES simulation of a diesel-like reacting spray. *Comput & Fluids* 2020;200.
- [23] Reitz RD, Diwakar R. Effect of drop breakup on fuel sprays. *SAE Tech Paper Ser* 1986;860469:1–10.
- [24] Chishty MA, Bolla M, Hawkes ER, Pei Y, Kook S. Soot formation modelling for n-dodecane sprays using the transported PDF model. *Combust Flame* 2018;192:101–19.
- [25] Pang KM, Jangi M, Bai X-S, Schramm J. Evaluation and optimization of phenomenological multi-step soot model for spray combustion under diesel engine-like operating conditions. *Combust Theory Model* 2015;19(3):279–308.
- [26] Liu K, Haworth DC, Yang X, Gopalakrishnan V. Large-eddy simulation of motored flow in a two-valve piston engine: POD analysis and cycle-to-cycle variations. *Flow Turbul Combust* 2013;91(2):1–31.
- [27] Senecal PK, Pomraning E, Richards KJ, Som S. An investigation of grid convergence for spray simulations using an LES turbulence model. *SAE Tech Paper* 2013;01–1083.
- [28] Yao T, Pei Y, Zhong B-J, Som S, Lu T, Luo KH. A compact skeletal mechanism for n-dodecane with optimized semi-global low-temperature chemistry for diesel engine simulations. *Fuel* 2017;191:339–49.
- [29] Pang KM, Karvounis N, Walther JH, Schramm J, Glarborg P, Mayer S. Modeling of temporal and spatial evolution of sulphur oxides and sulphuric acid under large, two-stroke marine engine-like conditions using integrated CFD-chemical kinetics. *Appl Energy* 2017;193:63–73.
- [30] Pang KM, Karvounis N, Walther JH, Schramm J. Numerical investigation of soot formation and oxidation processes under large two-stroke marine diesel engine-like conditions using integrated CFD-chemical kinetics. *Appl Energy* 2016;169:874–87.

- [31] Pei Y, Som S, Pomraning E, Senecal PK, Skeen SA, Manin J, Pickett LM. Large eddy simulation of a reacting spray flame with multiple realizations under compression ignition engine conditions. *Combust Flame* 2015;162:4442–55.
- [32] Zhang M, Ong JC, Pang KM, Bai X-S, Walther JH. An investigation on early evolution of soot in n-dodecane spray combustion using large eddy simulation. *Fuel* 2021;293:120072.
- [33] Jangi M, Yu R, Bai X-S. Development of chemistry coordinate mapping approach for turbulent partially premixed combustion. *Flow Turbul Combust* 2013;90(2):285–99.
- [34] Jangi M, Bai X-S. Multidimensional chemistry coordinate mapping approach for combustion modelling with finiterate chemistry. *Combust Theory Model* 2012;16: 1109–1032.
- [35] Jangi M, Altarawneh M, Glugogorski BZ. Large-eddy simulation of methanol pool fires using an accelerated stochastic fields method. *Combust Flame* 2016;173:89–98.
- [36] Fernandez SF, Paul C, Sircar A, Imren A, Haworth DC, Roy S, Modest MF. Soot and spectral radiation modeling for high-pressure turbulent spray flames. *Combust Flame* 2018;190:402–15.
- [37] Pang KM, Poon HM, Ng HK, Gan S, Schramm J. Soot formation modeling of n-dodecane and diesel sprays under engine-like conditions. *SAE Trans* 2015.
- [38] Brookes S, Moss J. Predictions of soot and thermal radiation properties in confined turbulent jet diffusion flames. *Combust Flame* 1999;116:486–503.
- [39] Pang KM, Jangi M, Bai X-S, Walther JH, Schramm J. Modelling of diesel spray flames under engine-like conditions using an accelerated Eulerian stochastic fields method. *Combust Flame* 2018;183:363–83.
- [40] Pang KM, Jangi M, Bai X-S, Schramm J. Investigation of chemical kinetics on soot formation event of n-heptane spray combustion. *SAE Tech Paper* 2014;01–1054.
- [41] Engine Combustion Network, available from: <https://ecn.sandia.gov/ecn-data-search/>.
- [42] Pei Y, Hawkes ER, Kook S. A comprehensive study of effects of mixing and chemical kinetic models on predictions of n-heptane jet ignitions with the PDF method. *Flow Turbul Combust* 2013;91(2):249–80.
- [43] Manin J, Bardi M, Pickett LM, Payri R. Boundary condition and fuel composition effects on injection processes of high-pressure sprays at the microscopic level. *Int J Multiphase Flow* 2016;83:267–78.
- [44] Payri R, Viera JP, Gopalakrishnan V, Szymkowicz PG. The effect of nozzle geometry over the evaporative spray formation for three different fuels. *Fuel* 2017;188:645–60.
- [45] Kahila H, Wehrfritz A, Kaario O, Masouleh MG, Maes N, Somers B, Vuorinen V. Large-eddy simulation on the influence of injection pressure in reacting spray a. *Combust Flame* 2018;191:142–59.
- [46] Skeen SA, Manin J, Pickett LM, Cenker E, Bruneaux G, Kondo K, Aizawa T, Westlie F, Dalen K, Ivarsson A, et al. A progress review on soot experiments and modeling in the engine combustion network (ECN). *SAE Int J Engines* 2016;9(2):883–98.
- [47] Xu Z, Duan X, Liu Y, Deng B, Liu J. Spray combustion and soot formation characteristics of the acetone-butanol-ethanol/diesel blends under diesel engine-relevant conditions. *Fuel* 2020;280:118483.
- [48] Pachano L, Xu C, Garcia-Olivier JM, Pastor JM, Novella R, Kundu P. A two-equation soot-in-flamelet modeling approach applied under spray a conditions. *Combust Flame* 2021;231:111488.
- [49] Chemkin.Pro, available from: <https://www.ansys.com/products/fluids/ansys-chemkin-pro>.
- [50] Bao H, Maes N, Akargun HY, Somers B. Large eddy simulation of cavitation effects on reacting spray flames using FGM and a new dispersion model with multiple realizations. *Combust Flame* 2022;236:11764.